First-principles opacity table of warm dense deuterium for inertial-confinement-fusion applications

S. X. Hu (□□□), L. A. Collins, V. N. Goncharov, T. R. Boehly, R. Epstein, R. L. McCrory, and S. Skupsky

Phys. Rev. E **90**, 033111 — Published 23 September 2014

DOI: 10.1103/PhysRevE.90.033111

First-principles opacity table of warm dense deuterium for inertial confinement fusion applications

S. X. Hu (胡素兴)[1,*], L. A. Collins[2], V. N. Goncharov[1], T. R. Boehly[1], R. Epstein[1], R. L. McCrory[1,3], and S. Skupsky[1]

[1]Laboratory for Laser Energetics, University of Rochester, 250 E. River Road, Rochester, NY 14623-1299

[2]Theoretical Division, Los Alamos National Laboratory, Los Alamos, NM 87545

[3]also at Department of Physics and Astronomy and Department of Mechanical Engineering, University of Rochester

[*]Email: shu@lle.rochester.edu

Abstract

Accurate knowledge of the optical properties of warm dense deuterium–tritium (DT) is important for reliable design of inertial confinement fusion (ICF) implosions using radiation–hydrodynamics simulations. The opacity of a warm dense DT shell essentially determines how much radiation from hot coronal plasmas can be deposited in the DT fuel of an imploding capsule. Even for the simplest species of hydrogen, the accurate calculation of their opacities remains a challenge in the warm-dense matter (WDM) regime because strong-coupling and quantum effects play an important role in such plasmas. With quantum-molecular-dynamics (QMD) simulations, we have derived a first-principles opacity table (FPOT) of deuterium (and DT by mass scaling) for a wide

range of densities from $\rho_D = 0.5$ g/cm^3 to $\rho_D = 673.518$ g/cm^3 and temperatures from $T =$ 5000 K up to the Fermi temperature (T_F) for each density. Compared with results from the astrophysics opacity table (AOT) currently used in our hydrocodes, the FPOT of deuterium from our QMD calculations has shown a significant increase in opacity for strongly coupled and degenerate plasma conditions by a factor of 3 to 100 in the ICF-relevant photon-energy range. As conditions approach those of classical plasma, the opacity from FPOT converges to the corresponding values of AOT. By implementing the FPOT of deuterium/DT into our hydrocodes, we have performed radiation–hydrodynamics simulations for low-adiabat, cryogenic DT implosions on OMEGA and for direct-drive–ignition designs for the National Ignition Facility (NIF). The simulation results using FPOT showed that the target performance (in terms of neutron yield and energy gain) could vary from ~10% up to a factor of ~2 depending on the adiabat of the imploding DT capsule; the lower the adiabat, the more variation is seen in the prediction of target performance when compared to the AOT modeling.

PACS numbers: 52.25.Os, 52.27.Gr, 78.20.Ci

I. INTRODUCTION

Material properties of hydrogen and its isotopes [deuterium and tritium (DT)] are important in many fields such as astrophysics [1,2], planetary science [3,4], and inertial confinement fusion (ICF) [5–7]. Even though hydrogen is the simplest element in the universe, its static and dynamic properties under warm dense conditions are not well known. Warm-dense-matter (WDM) conditions normally refer to a density from several

to many times solid density and a temperature below the Fermi temperature (T_F) and are often encountered when studying the cores of massive planets [3,4] and the imploding shell of ICF targets [8].

In ICF implosions, a capsule consisting of a cryogenic deuterium–tritium (DT) layer covered by an ablator is initially compressed to the WDM regime by laser/x-ray shocks [5–7]. The subsequent inward motion (implosion) of the capsule leads to the final formation of a hot spot surrounded by a high-density but relatively cold shell because of the spherical convergence. The α-particle heating [9] within the hot spot, if strong enough to "bootstrap" the heat, can initiate the burn-wave propagation through the high-density shell. The burning of high-density DT plasmas [5,10] may result in a net energy gain at the end. To obtain larger compression (normally measured by the areal density ρR) at certain drive energy, the entropy of an imploding DT shell must be as low as possible. The lower entropy is normally characterized by a quantity called an "adiabat," which is conventionally defined as the ratio of pressure to the Fermi degeneracy pressure ($\alpha = P/P_F$). The lower the adiabat, the more the plasma becomes nonideal. Plasmas in such low-adiabat ($\alpha \leq 3$) implosions are readily within the WDM regime [8–11].

In the WDM regime, plasmas can consist of atoms, molecules, ions, and free electrons, in which many-body correlations and quantum effects play an important role in determining plasma properties. Because of these strong coupling and degeneracy effects, it remains a challenging task to accurately calculate the static, dynamic, and optical properties of warm dense hydrogen/deuterium. Accurate methods such as the path-integral Monte Carlo (PIMC) [12,13], quantum molecular dynamics (QMD) [14,15], and the coupled electron–ion Monte Carlo (CEIMC) [16] are required to understand such

complicated systems. On the experimental side, measurements of the Hugoniot and the optical reflection of shocked hydrogen and deuterium [17–24] provide benchmarks for state-of-art calculations [25–36] of the equation of state (EOS) and optical properties. These studies have advanced our understanding of hydrogen/deuterium properties under the warm dense conditions, which are routinely accessed by ICF implosions.

Because of their importance to astrophysics, planetary science, and ICF, the equation-of-state [25–36] and transport properties including thermal/electrical conductivities [29,37–43] of warm-dense hydrogen have been extensively investigated in recent years using first-principles methods. Significant differences in the properties of warm dense hydrogen have been identified for the strongly coupled and degenerate plasma conditions, when compared to semi-empirical models. Those studies have stimulated comprehensive investigations in EOS [30,31,33,35], electron–ion thermal equilibration [44–48], and thermal conductivity [43] for a much wider range of densities and temperatures that are closely relevant to ICF simulations. These first-principles results in EOS and thermal conductivity of warm dense DT have improved the accuracy of ICF simulations.

The other important piece of physics to consider for accurately modeling ICF is the optical properties of DT in the WDM regime. Designing and understanding ICF implosions rely on radiation–hydrodynamics simulations in which radiation transport is necessary for accurate modeling. The precise opacity of warm dense DT plasmas is therefore needed to understand the transport of the radiation emitted from hot coronal plasmas to the imploding shell. In particular, the DT opacity determines the amount of radiation energy deposited into the warm DT shell, thereby controlling the radiation

preheat in the implosion, especially for direct-drive thin-layer ablators used to reduce the target mass for high-velocity implosions. In the latter case, the warm DT layer may be directly exposed to coronal radiations once the thin ablator vanishes.

Historically, the opacity of hydrogen has been extensively studied in the astrophysics community since it is important for understanding the emission of stars and the light absorption of the interstellar media [1,2]. Such astrophysics opacity tables (AOT's) [49] were built in the 1970s using atomic models. Some recent examples are the OPAL project [50] and the Opacity Library (OPLIB) [51]. Although improvements have been continuously made to these opacity tables over the years, they are essentially built from atomic models, in which many-body correlations and quantum effects in such non-ideal plasmas are approximately taken into account. Most importantly, because of the validity of models, these astrophysics opacity tables may not accurately portray the WDM regime. For instance, the AOT of DT currently used in our hydrocodes had available data points only to a certain low-temperature limit for a given density; the mass-absorption coefficients of cold DT were patched into the opacity at temperatures below such limits. It is therefore natural to ask how such an incomplete AOT could affect ICF simulations. Since the first-principles methods have been advanced in recent years, they might be applied to accurately calculate the opacity of warm dense plasmas.

In this article, we present such a first-principles opacity table (FPOT) of deuterium calculated using the QMD method. The wide range of deuterium densities, from ρ = 0.5 g/cm^3 to ρ = 673.518 g/cm^3, covers the typical density conditions undergone by ICF implosions. The temperatures have been sampled from T = 5000 K up to the Fermi temperature for each density point. The resulting FPOT has been compared

with the AOT currently used in our hydro-codes. We found that the QMD opacity of deuterium is higher than the patched AOT in the low-temperature regime by a factor of 3 to 100, depending on the photon-energy range. When the plasma temperature approaches the Fermi temperature, the FPOT converges to AOT near the classical plasma boundary. Implementing the FPOT into our hydro-codes, we have examined the opacity effects in ICF implosions through radiation–hydrodynamics simulations. The simulations using FPOT indicated that the target performance could vary from ~10% up to a factor of ~2 for low-adiabat ($\alpha \leq 3$) ICF targets, when compared with the traditional AOT modeling. The lower the target entropy, the more opacity effects can be seen in predicting target performance.

This article is organized as follows: The QMD method is laid out in Sec. II. The details of opacity calculation are described in Sec. III, with accompanying comparisons between the FPOT and the AOT and the Drude model for densities and temperatures typical of an ICF imploding shell. Some EOS comparisons with other calculations are also done in Sec. III. Section IV describes radiation–hydrodynamics simulations that we performed using the FPOT of deuterium/DT for both direct-drive implosions on OMEGA and two ICF designs for the National Ignition Facility (NIF). The opacity effects on ICF target performance are discussed in detail. Finally, our summary is presented in Sec. V.

II. THE QUANTUM-MOLECULAR-DYNAMICS (QMD) METHOD

To investigate the optical response of warm dense deuterium, we consider the plasma as a many-electron system, which is described by a wave function $\Psi(\mathbf{r}_1,\mathbf{r}_2,...,\mathbf{r}_N)$.

The wave function satisfies the following Schrödinger equation (atomic units used throughout):

$$\left[-\frac{1}{2}\sum_i \Delta_i + \sum_i V(\mathbf{r}_i) + \sum_{i\neq j}\frac{1}{|\mathbf{r}_i-\mathbf{r}_j|}\right]\Psi = E\Psi. \tag{1}$$

The second term in Eq. (1) is the electron–ion interaction, while the third term describes the Coulomb repulsion among electrons. A tractable way to solve the above Schrödinger equation is to map the many-electron wave function onto a "one-electron" basis $\Psi(\mathbf{r}_1,\mathbf{r}_2,...,\mathbf{r}_N) \rightarrow [\psi_1(\mathbf{r}_1),\psi_2(\mathbf{r}_2),...,\psi_N(\mathbf{r}_N)]$. The Kohn–Sham density functional theory (DFT) [52,53] is just one of such efficient "mean-field" theories of a many-electron system, in which the total wave function takes a product form of an individual one-electron "orbital" $\psi_i(\mathbf{r})$. By doing so, Eq. (1) can be cast into the Kohn–Sham (KS) equation for $\psi_i(\mathbf{r})$:

$$\left[-\frac{1}{2}\Delta + V_z(\mathbf{r}) + V_{\mathrm{H}}(\rho)(\mathbf{r}) + V_{\mathrm{xc}}(\rho)(\mathbf{r})\right]\psi_i(\mathbf{r}) = \epsilon_i\psi_i(\mathbf{r}), \tag{2}$$

with the electron density and the Hartree term defined as

$$\rho(\mathbf{r}) = \sum_{i=1}^{N}|\psi_i(\mathbf{r})|^2; \quad V_{\mathrm{H}}(\rho)(\mathbf{r}) = \int\frac{\rho(\mathbf{r}')}{|\mathbf{r}-\mathbf{r}'|}\mathrm{d}r'. \tag{3}$$

The terms of $V_z(r)$ and $V_{xc}(r)$ in Eq. (2) are the Coulomb potential between electrons and ions and the exchange potential among electrons, respectively. Since the exchange-correlation term V_{xc} and the Hartree term (V_H) depend on the electron density $\rho(\mathbf{r})$, which is again a function of $\psi(\mathbf{r})$, the Kohn–Sham equation can be solved in a self-consistent (i.e., *iterative*) way. We obtain a similar KS eigenvalue equation within the first Brillouin zone for each reciprocal wave-vector k as prescribed by the Bloch's theorem. Together with the ionic force, the resulting electronic force is then used to move the classical ions according to the classical Newton's equation under the Born–Oppenheimer approximation [14,15] for a QMD step.

Our QMD simulations have been performed within the Mermin finite temperature DFT [54], which was implemented in the Vienna *ab initio* simulation package (VASP) [55,56] using a plane-wave basis. The generalized gradient approximation (GGA) along with the Perdew–Burke–Ernzerhof (PBE) exchange-correlation functional [57] is employed in our QMD simulations. The electron–ion interaction is modeled by the projector augmented wave (PAW) pseudopotentials for deuterium mass densities below ρ_D = 15.709 g/cm^3; while for high-density points (ρ_D > 15.709 g/cm^3) in which smaller inter-particle distance may invalidate the use of PAW pseudopotentials, the pure Coulombic potential is applied. To converge the QMD calculations, we have set the plane-wave cutoff energy to E_{max} = 700 eV for low-density points and E_{max} = 1000 to 8000 eV for high-density points. A periodically replicated cubic cell was used with the number of atoms varying from N = 128 to N = 1000 for different densities.

The system was assumed to be in local thermodynamical equilibrium with equal electron and ion temperatures ($T_e = T_i$). The isokinetic ensemble was used for our QMD

simulations in which the number of particles, volume, and temperature are kept constant. In a periodic boundary condition, the electron wave function can be described by the Bloch waves which are products of plane waves with different momenta (ħk) and a periodic function of space. Each k-point in the first Brillouin zone uniquely defines every Bloch state. For each QMD step, a set of electronic state functions for each *k* point was self-consistently determined for a given ionic configuration. Then the ions were moved classically with a velocity Verlet algorithm, according to the combined ionic and electronic forces. The ion temperature was kept constant through simple velocity scaling. We tested the Γ point (**k** = 0) sampling of the first Brillion zone by comparing it with calculations using large *k*-point sets. When we increased the *k*-point sets to 4 × 4 × 4 Monkhorst–Pack grid, the obtained results varied only ~2%. So for most of our calculations we employed the Γ-point sampling. A large number of energy bands (plane waves up to N_b = 5000) were included in the molecular dynamics (MD) propagation to ensure that the population on the highest-energy band be as low as 10^{-5}. The MD time step was chosen to be $\delta t \le r_S \Big/ \left(20\sqrt{kT/M_D}\right)$ with the Wagner-Seitz radius $r_S = (3/4\pi n_i)^{1/3}$, temperature T, and the mass M_D of deuterium ion. This choice of time step guaranteed a good convergence in our QMD calculations.

A set of self-consistent ion trajectories and electronic wave functions result from such QMD time propagations. These trajectories provide a consistent set of static, dynamic, and optical properties of warm dense deuterium. The EOS quantities (pressure and internal energy) of warm dense deuterium can be obtained in a straightforward fashion from the QMD simulations; while for dynamic and optical properties, one must

post-process the QMD trajectories by evaluating the velocity dipole matrix elements, discussed in the next section.

III. FPOT OF WARM DENSE DEUTERIUM

A. Procedures for optical-property calculations

The electrical and thermal conduction properties of warm dense plasmas can, in principle, be calculated by evaluating the velocity dipole matrix elements D_{mn} from the VASP wave functions for the uncorrelated snapshots of the ionic configurations. The quantity D_{mn} was then used to compute the frequency-dependent Onsager coefficients within the Kubo–Greenwood formalism [58]:

$$L_{ij}(\omega) = \frac{2\pi(-e)^{4-i-j}}{3Vm_e^2\omega} \sum_{mn} \mathrm{F}_{mn} \left|D_{mn}\right|^2 \times \left(\frac{E_m + E_n}{2} - H\right)^{i+j-2} \delta(E_m - E_n - \hbar\omega), \tag{4}$$

where $V = 1/\rho$ is the atomic volume, $E_m(E_n)$ is the energy of the mth (nth) state, and H is the enthalpy (per atom) of the system. The quantity of F_{mn} is the difference between the Fermi–Dirac distributions for states m and n at temperature T. The δ function in the above equation is approximated by a Gaussian function with a width of ~0.1 eV. The Onsager coefficients essentially determine the transport and optical properties of the system.

For example, to calculate the frequency-dependent absorption coefficient $\alpha_K(\omega)$, we need only the electric conductivity and the index of refraction. The procedure is as

follows: from the real part of the electric conductivity, $\sigma_1(\omega) = L_{11}(\omega)$, the imaginary part of the electric conductivity can be obtained from the principal value integral:

$$\sigma_2(\omega) = -\frac{2}{\pi} P\left(\int \frac{\omega \sigma_1(\omega')}{\omega'^2 - \omega^2} \mathrm{d}\omega' \right). \tag{5}$$

The dielectric function $\varepsilon(\omega) = \varepsilon_1(\omega) + i\,\varepsilon_2(\omega)$ can be calculated by

$$\begin{aligned} \varepsilon_1(\omega) &= 1 - \frac{4\pi}{\omega}\sigma_2(\omega) \\ \varepsilon_2(\omega) &= \frac{4\pi}{\omega}\sigma_1(\omega) \end{aligned} \tag{6}$$

Using the dielectric function, one can obtain the real [$n(\omega)$] and imaginary [$k(\omega)$] parts of the refraction index:

$$\begin{aligned} n(\omega) &= \sqrt{\frac{|\varepsilon(\omega)| + \varepsilon_1(\omega)}{2}} \\ k(\omega) &= \sqrt{\frac{|\varepsilon(\omega)| - \varepsilon_1(\omega)}{2}} \end{aligned} \tag{7}$$

The frequency-dependent reflectivity is given by

$$R(\omega) = \frac{\left[n(\omega) - n_0\right]^2 + k(\omega)^2}{\left[n(\omega) + n_0\right]^2 + k(\omega)^2}. \tag{8}$$

with n_0 = 1 for vacuum. Finally, the mass absorption coefficient (α_m) is equal to the absorption coefficient (α_K) divided by the mass density [59], i.e.,

$$\alpha_m(\omega) = \frac{\alpha_K(\omega)}{\rho} = \frac{4\pi\bar{\sigma}_1(\omega)}{c \times \bar{n}(\omega)} \times \frac{1}{\rho}, \tag{9}$$

where c is the speed of light. The "bar" over σ_1 and n stands for averaging over the uncorrelated snapshots being sampled. We found that five to ten snapshots generally give a good statistic with a variation less than ~5%. It is noted that a larger number of energy bands, two to three times larger than those used in the molecular dynamics propagations, is required in the snapshot calculations, making enough empty bands available to converge toward an accurate evaluation of D_{mn}.

Under the multigroup diffusion approximation, the Rosseland mean opacity K_R was used for the radiation transport in hydrodynamics simulations. In general, the grouped Rosseland and Planck mean opacities were calculated by

$$K_R(\omega_1 : \omega_2) = \frac{\int_{\omega_1}^{\omega_2} n(\omega)^2 \frac{\partial B(\omega,T)}{\partial T} d\omega}{\int_{\omega_1}^{\omega_2} n(\omega)^2 \frac{1}{\alpha_m(\omega)} \frac{\partial B(\omega,T)}{\partial T} d\omega} \tag{10}$$

$$K_P(\omega_1 : \omega_2) = \frac{\int_{\omega_1}^{\omega_2} n(\omega)^2 \alpha_m(\omega) B(\omega,T) d\omega}{\int_{\omega_1}^{\omega_2} n(\omega)^2 B(\omega,T) d\omega} \tag{11}$$

for a group of photon energies between $\hbar\omega_1$ and $\hbar\omega_2$. Here, the Planck function $B(\omega,T) = \left(\hbar\omega^3 / 4\pi^3 c^2\right) \times 1 \Big/ \left(e^{\hbar\omega/k_B T} - 1\right)$ depends on the emitted photon energy and the plasma temperature. We obtained the total Rosseland mean opacity for ω_1 = 0 and $\omega_2 = \infty$.

B. Reflectivity and EOS comparisons with experiments and other calculations

Although no experimental data exists for the opacities of warm dense deuterium, we can indirectly benchmark the efficacy of the DFT-MD simulations by comparing them to other measured properties such as the reflectivity and the equation of state along the principal shock Hugoniot. For the static properties of warm dense deuterium, we compared the EOS in Fig. 1 for densities of [(a) and (b)] ρ_D = 1.0 g/cm^3 and [(c) and (d)] ρ_D = 10.0 g/cm^3 at different temperatures. The pressures as a function of plasma temperature are plotted in Figs 1(a) and 1(c), while the corresponding internal energies are shown in Figs. 1(b) and 1(d), respectively, for the two densities. The solid red circles represent the current QMD calculations, which are compared with both the previous PIMC results [8, 30] (open blue squares) and the recent QMD-OFMD (orbital-free molecular-dynamics) calculations (open green diamonds) by Wang *et al*. [35]. It is noted that the internal energy is referenced to the ground-state energy (E_0 = –15.886 eV) of D_2 molecule. Figure 1 shows that our QMD results using VASP agree very well with the QMD-OFMD calculations, which used the *ABINIT* code [60] for all range of temperatures explored. The PIMC simulations gave almost identical EOS results to the current QMD calculations for $T > 0.2 \times T_F$, while for the low-temperature regime, the PIMC simulations slightly overestimated the pressures. This is because as the plasma temperature decreases, the "Fermi-sign" problem [61] in PIMC prevents an accurate evaluation of degeneracy effects. The overall agreement among the various theoretical prescriptions yields a necessary if not sufficient validation of the present approach. Comparisons with experimental reflectivity provide a more stringent constraint.

In a recent paper [43], we demonstrated excellent agreement for the reflectivity of deuterium along the principal Hugoniot between QMD calculations using DFT and two experiments from the NOVA [19] and OMEGA [62] facilities. Since the reflectivity and opacity depend on the same basic optical properties [Eqs. (8) and (9)], this comparison gives a much stronger validation of the theoretical approach than the EOS.

C. FPOT comparison with opacity models

The first-principles QMD calculations have been performed for a wide range of deuterium densities from ρ = 0.5 g/cm^3 to ρ = 673.518 g/cm^3. The temperatures have been sampled from T = 5000 K up to the Fermi temperature $\left[T_{\mathrm{F}} = \hbar^2 \left(3\pi^2 n_e\right)^{2/3} \Big/ \left(2 m_{\mathrm{e}} k_{\mathrm{B}}\right) \right]$ for each density point. Here, k_{B} is the Boltzmann constant, and m_{e} and n_{e} are the electron mass and the number density of electrons, respectively. These density and temperature points fully cover the typical shell conditions in ICF implosions. Since finite number of energy bands are used in any QMD simulations, the maximum accessible energies for D_{mn} calculations are limited to certain values. Convergence tests on the absorption coefficient of deuterium at ρ_D=5.388 g/cm^3 and T=125000 K, with different number of energy bands n=1000, 2000, and 3000, indicate no difference in $\alpha(\omega)$ for photon energies up to $\hbar\omega$ ~150 eV and the high-energy tail extends naturally with the increase of energy bands. In general, calculations with more energy bands guarantee an extended high-energy tail for better fitting to large $\hbar\omega$ outside the directly-available energies. Namely, we had a frequency limit (ω_m) below which all the frequency-dependent quantities can be directly computed from the QMD

simulations. For $\omega > \omega_m$, the electric conductivity σ_1 can be obtained by numerically fitting its high-frequency tail [63] with the following function form:

$$\sigma_1(\omega > \omega_m/2) = \frac{a_1}{a_2 + a_3\omega^2 + a_4\omega^{3.2}} \tag{12}$$

with the fitting parameters a_1, a_2, a_3, and a_4. These parameters are numerically determined using least-square fitting for each ρ/T condition. This fitting form incorporates both the Drude term of $\sim\omega^2$ for low-photon energies [64] and the extra term of $\omega^{3.2}$ that is similar to the $\sim\omega^3$ behavior in Kramers' free-free opacity of classical plasmas at the high photon-energy limit. The above fitting formula recovers the high-frequency dependence seen under classical plasma conditions.

As an example, Fig. 2 shows the absorption coefficient α_K as a function of frequency (photon energy) for three density/temperature conditions of warm dense deuterium plasmas. The solid red line and dashed green line represent the deuterium density at $\rho_D \approx 5.388$ g/cm^3 but different temperatures of $T \approx 10.8$ eV (125,000 K) and $T \approx 43.1$ eV (500,000 K), respectively. One sees that the increase in temperature slightly reduces the absorption coefficient for $h\nu > k_B T_F$ (indicated by the inset in Fig. 2, $T_F \approx$ 50.1 eV for this density). This is mainly caused by the decrease of F_{mn} in Eq. (4) as a result of the reduction of population in energy bands of $E_n < E_F$ as $T \to T_F$. For the low-photon energy regime ($h\nu < k_B T_F$), the population depletion in $E_n < E_F$ energy bands at $T = 43.1$ eV starts to contribute to the photoabsorption within these energy bands. This is

in contrast to the more degenerate case of T = 10.8 eV, for which most energy bands of $E_n < E_F$ are fully occupied so that photoabsorption with both initial and final states inside these energy bands is impossible [e.g., $F_{mn} \approx 0$ in Eq. (4)]. This explains the enhanced absorption in the low photon-energy regime ($h\nu < k_B T_F$) with the increase in plasma temperature. For the higher density of $\rho_D \approx 199.561$ g/cm^3 at $T \approx 43.1$ eV (500,000 K), the dashed–dotted blue line in Fig. 2 shows an approximately two orders of magnitude increase in absorption for $h\nu > 400$ eV, when compared to the low-density ($\rho_D \approx 5.388$ g/cm^3) case. The absorption coefficient does not increase linearly with $\sim\rho$ as for the free–free transition in classical plasma, but scales roughly as $\sim\rho^{3/2}$. Finally, the steep increase in photon absorption coefficients at $h\nu \approx 300$ eV for the $\rho_D \approx 199.561$-g/cm^3 case ($h\nu \approx 50$ eV for the $\rho_D \approx 5.388$-g/cm^3 case) is due to the minima in the refraction index $n(\omega)$ [see Eq. (9)], at which the radiation frequency is equal to the plasma frequency.

To further understand how much the WDM system resembles a metal, we have used the Drude model [64] to study the conduction properties of warm dense deuterium. In this model, the frequency-dependent electrical conductivity behaves as

$$\sigma_1(\omega) = \sigma_{dc} \Big/ \left(1 + \omega^2 \tau^2\right),$$

where τ is the collisional relaxation time and $\sigma_{dc} = \sigma_1(0)$ is the dc conductivity. From these quantities, we can estimate the electron density $n_e = \left(m_e \sigma_{dc}\right) \Big/ \left(e^2 \tau\right)$ and, in turn,

the ionization fraction $Z^* = (n_e V)/N_i$, where m_e and e are the electron mass and charge, respectively; V is the supercell volume; and N_i is the number of ions in V. Similarly, the Drude formulation gives expressions for the real and imaginary parts of the dielectric function

$$\epsilon_1(\omega) = 1 - \frac{\omega_p^2 \tau^2}{\omega_p^2 \tau^2 + 1}$$

$$\epsilon_2(\omega) = \frac{\omega_p^2 \tau^2}{\omega_p \tau \left(\omega_p^2 \tau^2 + 1\right)},$$

with the plasma frequency given by $\omega_p^2 = 4\pi n_e e^2 / m_e$. We can extract the quantities (τ, σ_{dc}, and ω_p) by performing a nonlinear least squares fit to either the frequency-dependent real electrical conductivity $\sigma_1(\omega)$ or to the dielectric functions. As an example, we consider deuterium at ρ=5.388 g/cm^3 and T = 125,000 K. Figure 3(a) displays the real part of the electrical conductivity as a function of photon energy for a QMD simulation (solid black line). A fit to the Drude form (dashed–dotted red line) yields σ_{dc} = 3.8 × 10^6 S/m and τ = 0.086 fs. These quantities, in turn, give n_e = 1.61 × 10^{24} electrons/cm^3 and ω_p = 7.14 × 10^{16} rad/s^{-1}; therefore Z^* = 1 indicates a fully ionized system. Using the τ and ω_p determined from the above equation, we calculate the Drude dielectric functions and, in turn, the components of the index of refraction and, therefore, the absorption coefficient. In Fig. 3(b), we present the resulting Drude absorption as well as the QMD

result. We note that the Drude absorption is not a fit but arises from the use of the Drude parameters in the optical formulae. The agreement at low photon energies (frequencies) is very good as expected. The Drude form eventually fails at high frequencies due to its failure to give the Kramers' frequency dependence in free-free transitions. The QMD reflectivity of the plasma is shown in Fig. 3(c), which has a dramatic rise below the plasma frequency ($\hbar\omega_p \approx 49$ eV) indicating a highly reflective metal and the inability to propagate low-frequency radiation ($h\nu < \hbar\omega_p$) within the plasma.

For the deuterium density of $\rho_D \approx 5.388$ g/cm^3, the total Rosseland mean opacities (K_R) from our QMD calculations are plotted by red circles as a function of the plasma temperature in Fig. 4. Results from the AOT [49] are also shown for comparison by blue squares. Figure 4 shows that as the plasma temperature increases to above ~35 eV and approaches the Fermi temperature ($T_F \approx 50.1$ eV for this density), the QMD opacity converges to AOT as what is expected. At low temperatures ($T < 20$ eV), however, significant differences are seen between the QMD results and the cold-opacity-patched AOT table. For this density, the actual model-calculated data in AOT reached only a temperature of $T \approx 25$ eV, and the cold opacities had been patched in for the low-T points ($T < 25$ eV), which significantly underestimated the opacity of warm dense plasmas. This is understandable since as deuterium is compressed to this density (>25× compression from solid D_2) and warms to above ~10,000 K, energy gaps are filled, and the density of states increases so that photon absorptions become more probable than in the cold solid case. Although the QMD predictions also show a slightly decreasing opacity from $T \approx 5$ eV to $T \approx 1.35$ eV, they are still well above the cold opacity level at T

≈ 1.35 eV. This opacity enhancement can again be attributed to the energy gap closing and the density of states increasing as a result of high compression, which are absent in cold solid D_2.

Since the cold-opacity-patched AOT is currently used in our hydro-codes for radiation-transport simulations with the multi-group diffusion scheme, we compare in Fig. 5 the grouped opacities from QMD calculations and our currently used AOT for the deuterium density studied in Fig. 4. Figures 5(a) and 5(b) plot the grouped opacities as a function of the central photon energy in each group for plasma temperatures of T = 10.8 eV and T = 43.1 eV, respectively. At the low plasma temperature [Fig. 5(a)], the grouped opacities from QMD calculations become overall higher than the patched cold-opacity values. For photon-energy groups of $h\nu < 2$ keV (important to ICF), the QMD opacity is higher than cold-opacity-patched AOT by a factor of 3 to 100, depending on $h\nu$. When the plasma temperature increases to T = 43.1 eV [Fig. 5(b)], both QMD and AOT opacities agree over a wide range of photon energies except for the first group at $h\nu$ = 50 eV. The free–free opacity dominates in such high-T plasmas.

We further compare the total K_R from QMD calculations with AOT in Figs. 6 and 7 for a much higher density of $\rho_D \approx 199.561$ g/cm^3. Again, differences in the low-temperature regime (T < 100 eV) are also identified in the total Rosseland mean opacities; the two opacities converge at high plasma temperatures as expected. Figures 7(a) and 7(b) compare the corresponding grouped opacities between QMD and cold-opacity-patched AOT for temperatures of T = 43.1 eV and T = 172.3 eV, respectively. For the more strongly coupled and degenerate plasma regime at T = 43.1 eV, Fig. 7(a) indicates an opacity from QMD calculations two orders of magnitude higher

than the cold opacity that was patched in AOT. For a higher plasma temperature at T = 172.3 eV, both QMD and AOT give very similar opacities at $h\nu > 0.5$ keV [shown by Fig. 7(b)], even though some discrepancies are still seen in the lower photon energies ($h\nu$ ≈ 100 to 300 eV). This is attributed to the fact that the refraction index $n(\omega)$ was not taken into account in AOT.

IV. APPLICATION OF FPOT TO SIMULATIONS OF ICF IMPLOSIONS

The first-principles opacity tables (FPOT) of deuterium (both Rosseland and Planck mean) have been built from these QMD calculations for a wide range of densities (ρ_D = 0.5 to 673.518 g/cm^3) and temperatures (from T = 5000 K up to the Fermi temperature for each density point). For higher temperature points ($T > T_F$), we have taken the AOT data into the FPOT since the first-principles calculations reproduced the AOT data at high-T classical plasma conditions, as shown in Figs. 4 and 6. For compatibility with our hydro-codes, we have created a FPOT with 48 photon-energy groups. The 48-group FPOT of deuterium is listed in the Supplementary Material [65]; the Rosseland and Planck mean opacities are almost identical for all groups. In this section, we will examine how the accurate FPOT may affect ICF implosions by comparing with the AOT modeling.

As a first example, a cryogenic DT implosion on OMEGA was simulated using our one-dimensional hydrocode *LILAC* [66]. The cryo DT target had a diameter of ~860 μm, which consisted of a plastic ablator with a thickness of 8.3 μm and a 49-μm layer of DT ice. It was directly driven by the moderate-adiabat ($\alpha \approx 2.4$), triple-picket pulse shown in Fig. 8(a). The triple-picket pulses launch three coalescence shocks into

the target which help to precisely set up the implosion adiabat; and the main pulse accelerate the target to high implosion velocity. This kind of pulse shape has been extensively used in direct-drive implosions on OMEGA [67, 68]. The usual flux-limited thermal transport model was applied for these simulations. The FPEOS table [30] was employed for the fuel DT, while the *SESAME*-EOS [69] was used for the ablator materials. As the laser pulses irradiated on the plastic CH ablator, they launched shocks into the DT layer so that the DT fuel was brought to warm dense plasma conditions. Finally, the main pulse drove the capsule to implode and the DT fuel was compressed due to the spherical convergence and the shock bouncing back from the center. To quantify how the radiation emitted from the hot coronal plasmas affect the imploding shell, we plotted the hydro-simulated density and temperature profiles in Figs. 8(b) and 8(c) as a function of target radius, respectively, for two different times at t = 2.0 ns and t = 2.8 ns during the implosion. Figure 8(b) shows that at this early time the plastic CH has not been completely ablated away (see the CH density spike at the right edge); the DT layer behind the CH was therefore hardly affected by the coronal radiations because the remaining CH can still efficiently stop low-energy x rays. Therefore, the FPOT (solid red line) and AOT (dashed blue line) modelings give very similar density and temperature profiles at this time, even though the DT shell is in the strongly-coupled and degenerate plasma conditions. However, as the laser continuously interacts with the CH layer, the plastic CH will be gradually ablated away. The loss of such a mid-Z "shielding" CH layer will enable x-ray transport into the warm dense DT shell, which is exactly seen from the prediction of the simulations. Figure 8(c) displays the spatial density/temperature profiles for a later time t = 2.8 ns of the implosion. We see from Fig. 8(c) that the hydro-

simulation using FPOT has led to an increase in temperature and a decrease in density compared to the AOT due to the higher opacity in FPOT for x-ray energies below ~2 keV [see Fig. 5(a)], which results in more absorption of x rays from the corona. This behavior in the DT shell can have a consequence at the peak compression, which is shown by Fig. 8(d). One sees reductions in both the ion temperature within the hot spot and the peak density attained in the FPOT modeling. In the end, the neutron yield drops about ~15% [from 1.82×10^{14} (AOT) to 1.58×10^{14} (FPOT)]. The neutron-averaged $\langle \rho R \rangle$ varies by ~10% between FPOT and AOT simulations.

Next, we examine the opacity effects on two different direct-drive designs for the NIF. Figure 9(a) shows the first NIF design that uses a target of diameter $\phi = 3294$ μm with a 22-μm CH ablator and a 125-μm-thick DT layer. The triple-picket pulse [Fig. 9(b): total 1.6 MJ] drives the target implosion at a moderately high adiabat ($\alpha \approx 2.8$). The hydro-simulation results using both FPOT and AOT are compared in Fig. 10. Similar to the OMEGA implosion shown in Fig. 8, the FPOT modeling predicts a slightly lower density and higher temperature when compared to the AOT case, for the late stage of the implosion when the CH layer is ablated away [Fig. 10(a)]. In Fig. 10(b), we plot the minimum adiabat as a function of time for the two cases. We see that the less-transparent DT predicted by FPOT has indeed more radiation preheat than the modeling with AOT. That raises the minimum adiabat from $\alpha = 2.8$ to $\alpha = 3.3$ at the end of acceleration (t = 8.5 ns). At the peak compression, the FPOT modeling predicts a reduced performance of the implosion in terms of peak density and ion temperature, indicated by Fig. 10(c). Figure 10(d) shows the corresponding neutron yields in the two cases, for which the energy gain varies by ~10%.

To mitigate the possible two-plasmon–decay (TPD) instability [70–73], several mid-Z ablators and mid-Z–doped [74,75] CH have been considered for direct-drive ICF designs. High-density carbon (HDC) [76] is one of the ablator candidates. It is also noted that for HDC ablators pure-carbon plasmas in the hot corona radiate more x rays than the plastic CH case since the averaged ion charge has increased from $\langle Z \rangle = 3.5$ (CH) to $\langle Z \rangle = 6$ (C). So, to better predict how much radiation may be deposited in the DT layer, the more-accurate FPOT is needed. In Fig. 11, we show hydro simulations of a NIF design using a thin-layer HDC ablator. As indicated by Fig. 11(a), the target consists of a 10-μm HDC layer and a thicker DT layer of 180 μm. Driven by the laser pulse (1.2 MJ) depicted in Fig. 11(b), the imploding DT shell has a moderately low implosion velocity of $v_{\text{imp}} = 3.4 \times 10^7$ cm/s. The capsule is set to a relatively lower adiabat of $\alpha \approx 1.8$. This means that the DT plasmas are in more strongly coupled and degenerate conditions, where the opacity difference between FPOT and AOT becomes bigger. Figure 11(c) compares the density and ion-temperature profiles at peak compression. These two simulations predict a peak density variation from $\rho_{\text{p}} = 405$ g/cm^3 (AOT) to $\rho_{\text{p}} = 348$ g/cm^3 (FPOT), and the maximum ion temperature changes from $T_{\text{i}} = 15.1$ keV (AOT) to $T_{\text{i}} = 13.5$ keV (FPOT). Again, the drop in peak density and ion temperature in the FPOT modeling results in the degradation of target performance. As shown by Fig. 11(d), the neutron yield is reduced from 3.2×10^{18} (AOT) to $\sim 1.5 \times 10^{18}$ (FPOT). For this lower-adiabat implosion, the target performance variation reaches a factor of ~2 between FPOT and AOT modelings. The accurate FPOT should be important for fine-tuning NIF target designs, especially for lower-adiabat ($\alpha \leq 2$) implosions. Finally, we have noticed that both FPOT and AOT give similar results for high-adiabat ($\alpha \geq 4$) implosions. Also, increasing the ablator

thickness could efficiently shield the radiation preheat in the DT fuel, although the penalty would be to implode an extra mass of ablator, which is useless for fusion.

V. SUMMARY

Using the QMD simulations, we have investigated the opacity of warm dense deuterium for a wide range of densities from $\rho_D = 0.5$ to 673.518 g/cm^3 and temperatures from $T = 5000$ K to the Fermi temperature for each density point. Significant differences between the QMD-calculated opacities and the cold opacities being patched in the astrophysics opacity table (AOT) have been identified for the strongly coupled and degenerate plasma conditions. The opacity of warm dense deuterium is higher than the cold opacity by a factor of ~3 to 100 in the ICF-relevant photon-energy range. This is attributed to both the increasing density of states related to compression and the temperature-induced depletion of state populations below the Fermi level. As the plasma temperature increases to near the Fermi temperature, however, the QMD opacities converge to AOT as expected. From these QMD calculations, we have constructed first-principles opacity tables (FPOT) for deuterium and deuterium–tritium (by mass scaling), which cover typical ICF plasma conditions. The multigroup FPOT of DT has been incorporated into our hydro-codes. The opacity effects have been demonstrated through radiation–hydrodynamics simulations of both OMEGA implosions and direct-drive NIF target designs. When compared to hydro simulations using FPOT, the AOT modeling generally underestimates the radiation preheat in thin-ablator ICF implosions. The predictions for ICF target performance could vary up to a factor of ~2 between AOT and FPOT modelings. The lower the adiabat of an ICF implosion, the more variations

observed. As a next step, we have begun a systematic comparison with the more recently developed OPLIB. We believe that the established first-principles opacity tables (FPOT) of hydrogen/deuterium/DT could be beneficial not only for the fine tuning of low-adiabat ICF target designs in future ignition attempts, but also for important applications in astrophysics. Finally, we hope these first-principles results could facilitate experimental efforts in measuring opacities of warm dense deuterium.

ACKNOWLEDGMENT

This material is based upon work supported by the Department of Energy National Nuclear Security Administration under Award Number DE-NA0001944, the University of Rochester, and the New York State Energy Research and Development Authority. The support of DOE does not constitute an endorsement by DOE of the views expressed in this article. This work was also supported by Scientific Campaign 10 at the Los Alamos National Laboratory, operated by Los Alamos National Security, LLC for the National Nuclear Security Administration of the U.S. Department of Energy under Contract No. DE-AC52-06NA25396.

REFERENCES

1. C. A. Iglesias, F. J. Rogers, and D. Saumon, Astrophys. J. Lett. **569**, L111 (2002).
2. G. Fontaine, P. Brassard, and P. Bergeron, Publ. Astron. Soc. Pac. **113**, 409 (2001).
3. N. C. Santos, W. Benz, and M. Mayor, Science **310**, 251 (2005).
4. S. Seager, Science **340**, 577 (2013).

5. S. W. Haan, J. D. Lindl, D. A. Callahan, D. S. Clark, J. D. Salmonson, B. A. Hammel, L. J. Atherton, R. C. Cook, M. J. Edwards, S. Glenzer, A. V. Hamza, S. P. Hatchett, M. C. Herrmann, D. E. Hinkel, D. D. Ho, H. Huang, O. S. Jones, J. Kline, G. Kyrala, O. L. Landen, B. J. MacGowan, M. M. Marinak, D. D. Meyerhofer, J. L. Milovich, K. A. Moreno, E. I. Moses, D. H. Munro, A. Nikroo, R. E. Olson, K. Peterson, S. M. Pollaine, J. E. Ralph, H. F. Robey, B. K. Spears, P. T. Springer, L. J. Suter, C. A. Thomas, R. P. Town, R. Vesey, S. V. Weber, H. L. Wilkens, and D. C. Wilson, Phys. Plasmas **18**, 051001 (2011).

6. D. D. Meyerhofer, R. L. McCrory, R. Betti, T. R. Boehly, D. T. Casey, T. J. B. Collins, R. S. Craxton, J. A. Delettrez, D. H. Edgell, R. Epstein, K. A. Fletcher, J. A. Frenje, Y. Y. Glebov, V. N. Goncharov, D. R. Harding, S. X. Hu, I. V. Igumenshchev, J. P. Knauer, C. K. Li, J. A. Marozas, F. J. Marshall, P. W. McKenty, P. M. Nilson, S. P. Padalino, R. D. Petrasso, P. B. Radha, S. P. Regan, T. C. Sangster, F. H. Séguin, W. Seka, R. W. Short, D. Shvarts, S. Skupsky, J. M. Soures, C. Stoeckl, W. Theobald, and B. Yaakobi, Nucl. Fusion **51**, 053010 (2011).

7. R. L. McCrory, R. Betti, T. R. Boehly, D. T. Casey, T. J. B. Collins, R. S. Craxton, J. A. Delettrez, D. H. Edgell, R. Epstein, J. A. Frenje, D. H. Froula, M. Gatu-Johnson, V. Y. Glebov, V. N. Goncharov, D. R. Harding, M. Hohenberger, S. X. Hu, I. V. Igumenshchev, T. J. Kessler, J. P. Knauer, C. K. Li, J. A. Marozas, F. J. Marshall, P. W. McKenty, D. D. Meyerhofer, D. T. Michel, J. F. Myatt, P. M. Nilson, S. J. Padalino, R. D. Petrasso, P. B. Radha, S. P. Regan, T. C. Sangster, F. H. Séguin, W. Seka, R. W. Short, A. Shvydky, S. Skupsky, J. M.

Soures, C. Stoeckl, W. Theobald, B. Yaakobi, and J. D. Zuegel, Nucl. Fusion **53**, 113021 (2013).

8. S. X. Hu, B. Militzer, V. N. Goncharov, and S. Skupsky, Phys. Rev. Lett. **104**, 235003 (2010).

9. O. A. Hurricane, D. A. Callahan, D. T. Casey, P. M. Celliers, C. Cerjan, E. L. Dewald, T. R. Dittrich, T. Döppner, D. E. Hinkel, L. F. Berzak Hopkins, J. L. Kline, S. Le Pape, T. Ma, A. G. MacPhee, J. L. Milovich, A. Pak, H.-S. Park, P. K. Patel, B. A. Remington, J. D. Salmonson, P. T. Springer, and R. Tommasini, Nature **506**, 343 (2014).

10. S. X. Hu, V. N. Goncharov, and S. Skupsky, Phys. Plasmas **19**, 072703 (2012).

11. L. Caillabet, S. Mazevet, and P. Loubeyre, Phys. Rev. B **83**, 094101 (2011).

12. C. Pierleoni, D. M. Ceperley, B. Bernu, and W. R. Magro, Phys. Rev. Lett. **73**, 2145 (1994).

13. B. Militzer and D. M. Ceperley, Phys. Rev. Lett. **85**, 1890 (2000).

14. L. Collins, I. Kwon, J. Kress, N. Troullier, and D. Lynch, Phys. Rev. E **52**, 6202 (1995).

15. J. G. Clérouin and S. Bernard, Phys. Rev. E **56**, 3534 (1997).

16. J. M. McMahon, M. A. Morales, C. Pierleoni, and D. M. Ceperley, Rev. Mod. Phys. **84**, 1607 (2012).

17. L. B. Da Silva, P. Celliers, G. W. Collins, K. S. Budil, N. C. Holmes, T. W. Barbee, Jr., B. A. Hammel, J. D. Kilkenny, R. J. Wallace, M. Ross, R. Cauble, A. Ng, and G. Chiu, Phys. Rev. Lett. **78**, 483 (1997).

18. G. W. Collins, L. B. Da Silva, P. Celliers, D. M. Gold, M. E. Foord, R. J. Wallace, A. Ng, S. V. Weber, K. S. Budil, and R. Cauble, Science **281**, 1178 (1998).

19. P. M. Celliers, G. W. Collins, L. B. Da Silva, D. M. Gold, R. Cauble, R. J. Wallace, M. E. Foord, and B. A. Hammel, Phys. Rev. Lett. **84**, 5564 (2000).

20. A. N. Mostovych, Y. Chan, T. Lehecha, A. Schmitt, and J. D. Sethian, Phys. Rev. Lett. **85**, 3870 (2000); A. N. Mostovych, Y. Chan, T. Lehecha, L. Phillips, A. Schmitt, and J. D. Sethian, Phys. Plasmas **8**, 2281 (2001).

21. M. D. Knudson, D. L. Hanson, J. E. Bailey, C. A. Hall, J. R. Asay, and W. W. Anderson, Phys. Rev. Lett. **87**, 225501 (2001); M. D. Knudson, D. L. Hanson, J. E. Bailey, C. A. Hall, and J. R. Asay, Phys. Rev. Lett. **90**, 035505 (2003).

22. V. E. Fortov, R. I. Ilkaev, V. A. Arinin, V. V. Burtzev, V. A. Golubev, I. L. Iosilevskiy, V. V. Khrustalev, A. L. Mikhailov, M. A. Mochalov, V. Y. Ternovoi, and M. V. Zhernokletov, Phys. Rev. Lett. **99**, 185001 (2007).

23. D. G. Hicks, T. R. Boehly, P. M. Celliers, J. H. Eggert, S. J. Moon, D. D. Meyerhofer, and G. W. Collins, Phys. Rev. B **79**, 014112 (2009).

24. P. Loubeyre, S. Brygoo, J. Eggert, P. M. Celliers, D. K. Spaulding, J. R. Rygg, T. R. Boehly, G. W. Collins, and R. Jeanloz, Phys. Rev. B **86**, 144115 (2012).

25. J. Clérouin and J.-F. Dufrêche, Phys. Rev. E **64**, 066406 (2001).

26. L. A. Collins, S. R. Bickham, J. D. Kress, S. Mazevet, T. J. Lenosky, N. J. Troullier, and W. Windl, Phys. Rev. B **63**, 184110 (2001).

27. B. Militzer, D. M. Ceperley, J. D. Kress, J. D. Johnson, L. A. Collins, and S. Mazevet, Phys. Rev. Lett. **87**, 275502 (2001).

28. M. P. Desjarlais, Phys. Rev. B **68**, 064204 (2003).

29. B. Holst, R. Redmer, and M. P. Desjarlais, Phys. Rev. B **77**, 184201 (2008).

30. S. X. Hu, B. Militzer, V. N. Goncharov, and S. Skupsky, Phys. Rev. B **84**, 224109 (2011).

31. L. Caillabet, S. Mazevet, and P. Loubeyre, Phys. Rev. B **83**, 094101 (2011).

32. L. A. Collins, J. D. Kress, and D. E. Hanson, Phys. Rev. B **85**, 233101 (2012).

33. M. A. Morales, L. X. Benedict, D. S. Clark, E. Schwegler, I. Tamblyn, S. A. Bonev, A. A. Correa, and S. W. Haan, High Energy Density Phys. **8**, 5 (2012).

34. J. Vorberger, D. O. Gericke, and W. D. Kraeft, High Energy Density Phys. **9**, 448 (2013).

35. C. Wang and P. Zhang, Phys. Plasmas **20**, 092703 (2013).

36. V. V. Karasiev, D. Chakraborty, O. A. Shukruto, and S. B. Trickey, Phys. Rev. B **88**, 161108(R) (2013).

37. V. Recoules, F. Lambert, A. Decoster, B. Canaud, and J. Clérouin, Phys. Rev. Lett. **102**, 075002 (2009).

38. F. Lambert, V. Recoules, A. Decoster, J. Clérouin, and M. Desjarlais, Phys. Plasmas **18**, 056306 (2011).

39. D. E. Hanson, L. A. Collins, J. D. Kress, and M. P. Desjarlais, Phys. Plasmas **18**, 082704 (2011).

40. B. Holst, M. French, and R. Redmer, Phys. Rev. B **83**, 235120 (2011).

41. C. E. Starrett, J. Clérouin, V. Recoules, J. D. Kress, L. A. Collins, and D. E. Hanson, Phys. Plasmas **19**, 102709 (2012).

42. C. Wang, Y. Long, X.-T. He, J.-F. Wu, W.-H. Ye, and P. Zhang, Phys. Rev. E **88**, 013106 (2013).

43. S. X. Hu, L. A. Collins, T. R. Boehly, J. D. Kress, V. N. Goncharov, and S. Skupsky, Phys. Rev. E **89**, 043105 (2014).

44. J. Daligault and G. Dimonte, Phys. Rev. E **79**, 056403 (2009).

45. L. X. Benedict, J. N. Glosli, D. F. Richards, F. H. Streitz, S. P. Hau-Riege, R. A. London, F. R. Graziani, M. S. Murillo, and J. F. Benage, Phys. Rev. Lett. **102**, 205004 (2009).

46. B. Xu and S. X. Hu, Phys. Rev. E **84**, 016408 (2011).

47. L. X. Benedict, M. P. Surh, J. I. Castor, S. A. Khairallah, H. D. Whitley, D. F. Richards, J. N. Glosli, M. S. Murillo, C. R. Scullard, P. E. Grabowski, D. Michta, and F. R. Graziani, Phys. Rev. E **86**, 046406 (2012).

48. C. Blancard, J. Clérouin, and G. Faussurier, High Energy Density Phys. **9**, 247 (2013).

49. W. F. Huebner, A. L. Merts, N. H. Magee, Jr., and M. F. Argo, Los Alamos National Laboratory, Los Alamos, NM, Report LA-6760-M (1977).

50. C. A. Iglesias and F. J. Rogers, Astrophys. J. **464**, 943 (1996).

51. J. Colgan, D. P. Kilcrease, J. Magee, N. H., G. S. J. Armstrong, J. Abdallah, J., M. E. Sherrill, C. J. Fontes, H. L. Zhang, and P. Hakel, AIP Conf. Proc. **1545**, 17 (2013).

52. P. Hohenberg and W. Kohn, Phys. Rev. **136**, B864 (1964).

53. W. Kohn and L. J. Sham, Phys. Rev. **140**, A1133 (1965).

54. N. D. Mermin, Phys. Rev. **137**, A1441 (1965).

55. G. Kresse and J. Hafner, Phys. Rev. B **47**, 558 (1993).

56. G. Kresse and J. Hafner, Phys. Rev. B **49**, 14251 (1994).

57. J. P. Perdew, K. Burke, and M. Ernzerhof, Phys. Rev. Lett. **77**, 3865 (1996); J. P. Perdew, K. Burke, and M. Ernzerhof, Phys. Rev. Lett. **78**, 1396(E) (1997).

58. R. Kubo, J. Phys. Soc. Jpn. **12**, 570 (1957); D. A. Greenwood, Proc. Phys. Soc. Lond. **71**, 585 (1958).

59. F. Perrot, Laser Part. Beams **14**, 731 (1996).

60. For details of the *ABINIT* code, please refer to http://www.abinit.org/.

61. D. M. Ceperley, Rev. Mod. Phys. **67**, 279 (1995).

62. T. R. Boehly, V. N. Goncharov, W. Seka, S. X. Hu, J. A. Marozas, D. D. Meyerhofer, P. M. Celliers, D. G. Hicks, M. A. Barrios, D. Fratanduono, and G. W. Collins, Phys. Plasmas **18**, 092706 (2011); T. R. Boehly, V. N. Goncharov, W. Seka, M. A. Barrios, P. M. Celliers, D. G. Hicks, G. W. Collins, S. X. Hu, J. A. Marozas, and D. D. Meyerhofer, Phys. Rev. Lett. **106**, 195005 (2011).

63. S. Mazevet, L. A. Collins, N. H. Magee, J. D. Kress, and J. J. Keady, Astron. Astrophys. **405**, L5 (2003).

64. N. W. Ashcroft and N. D. Mermin, *Solid State Physics*, College ed. (W.B. Saunders, Philadelphia, 1976).

65. See Supplemental Material at http://link.aps.org/supplemental/xxxx for the 48-group Planck and Rosseland opacity table (FPOT) of deuterium.

66. J. Delettrez, R. Epstein, M. C. Richardson, P. A. Jaanimagi, and B. L. Henke, Phys. Rev. A **36**, 3926 (1987).

67. V. N. Goncharov, T. C. Sangster, T. R. Boehly, S. X. Hu, I. V. Igumenshchev, F. J. Marshall, R. L. McCrory, D. D. Meyerhofer, P. B. Radha, W. Seka, S. Skupsky, C. Stoeckl, D. T. Casey, J. A. Frenje, R. D. Petrasso, Phys. Rev. Lett. **104**, 165001 (2010).

68. T. C. Sangster, V. N. Goncharov, R. Betti, P. B. Radha, T. R. Boehly, D. T. Casey, T. J. B. Collins, R. S. Craxton, J. A. Delettrez, D. H. Edgell, R. Epstein, C. J. Forrest, J. A. Frenje, D. H. Froula, M. Gatu-Johnson, V. Yu. Glebov, D. R. Harding, M. Hohenberger, S. X. Hu, I. V. Igumenshchev, R. Janezic, J. H. Kelly, T. J. Kessler, C. Kingsley, T. Z. Kosc, J. P. Knauer, S. J. Loucks, J. A. Marozas, F. J. Marshall, A. V. Maximov, R. L. McCrory, P. W. McKenty, D. D. Meyerhofer, D. T. Michel, J. F. Myatt, R. D. Petrasso, S. P. Regan, W. Seka, W. T. Shmayda, R. W. Short, A. Shvydky, S. Skupsky, J. M. Soures, C. Stoeckl, W. Theobald, V. Versteeg, B. Yaakobi, J. D. Zuegel, Phys. Plasmas **20**, 056317 (2013).

69. B. I. Bennett, J. D. Johnson, G. I. Kerley, and G. T. Rood, Los Alamos National Laboratory, Los Alamos, NM, Report LA-7130 (1978).

70. D. H. Froula, B. Yaakobi, S. X. Hu, P.-Y. Chang, R. S. Craxton, D. H. Edgell, R. Follett, D. T. Michel, J. F. Myatt, W. Seka, R. W. Short, A. Solodov, and C. Stoeckl, Phys. Rev. Lett. **108**, 165003 (2012).

71. D. T. Michel, A. V. Maximov, R. W. Short, S. X. Hu, J. F. Myatt, W. Seka, A. A. Solodov, B. Yaakobi, and D. H. Froula, Phys. Rev. Lett. **109**, 155007 (2012).

72. S. X. Hu, D. T. Michel, D. H. Edgell, D. H. Froula, R. K. Follett, V. N. Goncharov, J. F. Myatt, S. Skupsky, and B. Yaakobi, Phys. Plasmas **20**, 032704 (2013).

73. J. F. Myatt, H. X. Vu, D. F. DuBois, D. A. Russell, J. Zhang, R. W. Short, and A. V. Maximov, Phys. Plasmas **20**, 052705 (2013).

74. S. X. Hu, G. Fiksel, V. N. Goncharov, S. Skupsky, D. D. Meyerhofer, and V. A. Smalyuk, Phys. Rev. Lett. **108**, 195003 (2012).

75. G. Fiksel, S. X. Hu, V. N. Goncharov, D. D. Meyerhofer, T. C. Sangster, V. A. Smalyuk, B. Yaakobi, M. J. Bonino, and R. Jungquist, Phys. Plasmas **19**, 062704 (2012).

76. O. L. Landen, D. K. Bradley, D. G. Braun, V. A. Smalyuk, D. G. Hicks, P. M. Celliers, S. Prisbrey, R. Page, T. R. Boehly, S. W. Haan, D. H. Munro, R. G. Wallace, A. Nikroo, A. Hamza, J. Biener, C. Wild, E. Woerner, R. E. Olson, G. A. Rochau, M. Knudson, D. C. Wilson, H. F. Robey, G. W. Collins, D. Ho, J. Edwards, M. M. Marinak, B. A. Hammel, D. D. Meyerhofer, and B. J. MacGowan, J. Phys., Conf. Ser. **112**, 022004 (2008).

Figure captions

FIG. 1. (Color online) The EOS comparison of warm dense deuterium calculated by different first-principles methods (current QMD, PIMC [30] and QMD-OFMD [35]) for densities of [(a) and (b)] ρ_D = 1.0 g/cm^3 and [(c) and (d)] ρ_D = 10.0 g/cm^3.

FIG. 2. (Color online) The absorption coefficients of warm dense deuterium from QMD calculation are plotted as a function of photon energy for $\rho \approx$ 5.388 g/cm^3 and T = 125,000 K (solid red); $\rho_D \approx$ 5.388 g/cm^3 and T = 500,000 K (dashed green);and $\rho_D \approx$ 199.561 g/cm^3 and T = 500,000 K (dashed–dotted blue), respectively.

FIG. 3. (Color online) The QMD-calculated electrical conductivity (a) and absorption coefficient (b) as a function of photon energy, comparing with the Drude model for $\rho_D \approx$ 5.388 g/cm^3 and T = 125,000 K. The reflectivity from QMD calculations is also plotted in (c).

FIG. 4. (Color online) Comparisons of the total Rosseland opacity of deuterium at $\rho_D \approx$ 5.388 g/cm^3 as a function of the plasma temperature, between the QMD results (red circles) and the cold-opacity-patched AOT results (blue squares).

FIG. 5. (Color online) Comparisons of the 48-group Rosseland mean opacity between QMD and AOT as a function of the central photon energy in each group for deuterium of $\rho_D \approx$ 5.388 g/cm^3 at temperatures of (a) T = 10.8 eV and (b) T = 43.1 eV.

FIG. 6. (Color online) Comparisons of the total Rosseland opacity of deuterium at $\rho_D \approx$ 199.561 g/cm^3 as a function of the plasma temperature, between the QMD results (red circles) and the cold-opacity-patched AOT (blue squares).

FIG. 7. (Color online) Comparisons of the 48-group Rosseland mean opacity between QMD and AOT as a function of the group photon energy, for deuterium of $\rho_D \approx$ 199.561 g/cm^3 at two different temperatures of (a) $T = 43.1$ eV and (b) $T = 172.3$ eV.

FIG. 8. (Color online) The radiation–hydrodynamics simulation of an OMEGA cryogenic DT implosion ($\alpha = 2.4$) using FPOT (solid red line) is compared with the AOT modeling (dashed blue line): (a) the laser pulse shape; [(b), (c)] the density and electron-temperature profiles of the imploding shell at $t = 2.0$ ns and $t = 2.8$ ns, respectively; and (d) the density and ion-temperature profiles at peak compression ($t = 2.98$ ns).

FIG. 9. (Color online) (a) The schematic diagram of a direct-drive NIF target and (b) the laser pulse shape with a total energy of 1.6 MJ, which drives an $\alpha \approx 2.8$ implosion.

FIG. 10. (Color online) Comparisons of radiation–hydrodynamics simulations between FPOT and AOT modeling, for the direct-drive NIF design shown in Fig. 9: (a) the density and electron-temperature profiles of the imploding shell at $t = 8.5$ ns, (b) the minimum adiabat as a function of time, (c) the density and ion-temperature profiles at the beginning of burn ($t = 8.94$ ns), and (d) the neutron yield comparison.

FIG. 11. (Color online) Comparisons of radiation–hydrodynamics simulations between FPOT and AOT modeling for a lower adiabat $\alpha \approx 1.8$), direct-drive NIF design using a high-density–carbon (HDC) ablator: (a) the target dimensions, (b) the triple-picket laser pulse having a total energy of 1.2 MJ, (c) the density and ion-temperature profiles at the beginning of burn (t = 12.641 ns), and (d) a comparison of the neutron yields.

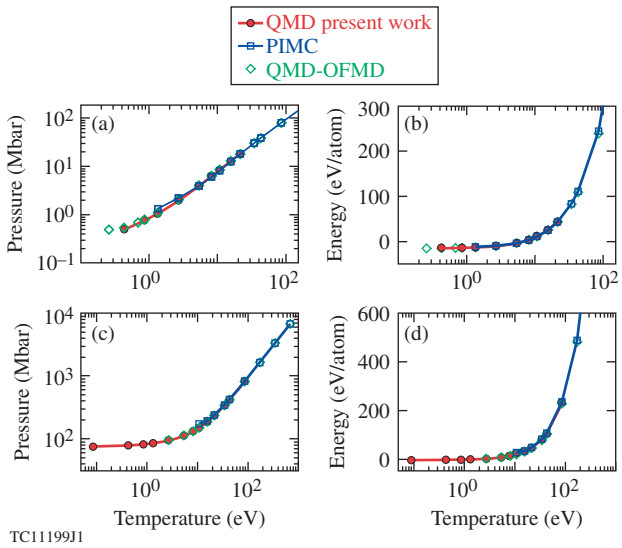

FIG. 1. (Color online) The EOS comparison of warm dense deuterium calculated by different first-principles methods (current QMD, PIMC [30] and QMD-OFMD [35]) for densities of [(a) and (b)] $\rho_D = 1.0$ g/cm^3 and [(c) and (d)] $\rho_D = 10.0$ g/cm^3.

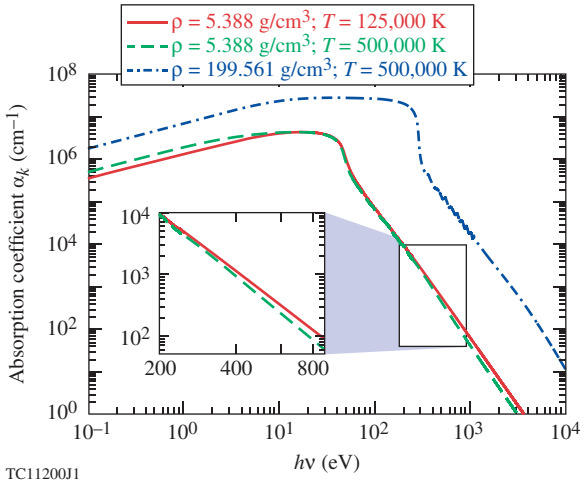

FIG. 2. (Color online) The absorption coefficients of warm dense deuterium from QMD calculation are plotted as a function of photon energy for $\rho \approx 5.388$ g/cm^3 and $T =$ 125,000 K (solid red); $\rho_D \approx 5.388$ g/cm^3 and $T = 500{,}000$ K (dashed green);and $\rho_D \approx$ 199.561 g/cm^3 and $T = 500{,}000$ K (dashed–dotted blue), respectively.

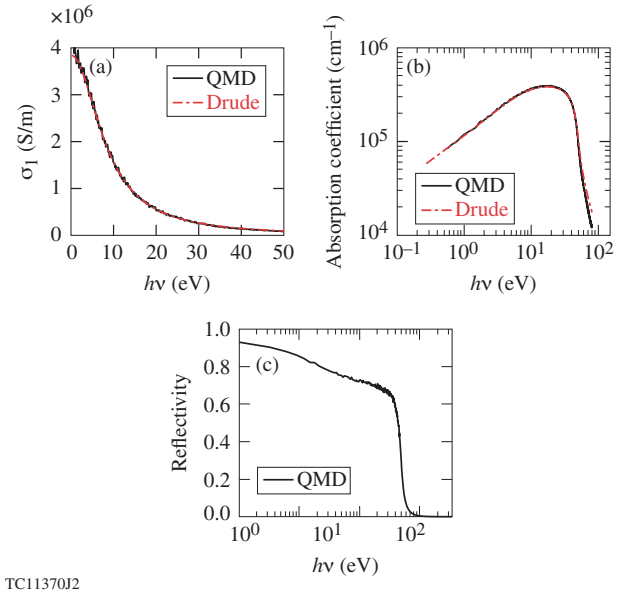

FIG. 3. (Color online) The QMD-calculated electrical conductivity (a) and absorption coefficient (b) as a function of photon energy, comparing with the Drude model for $\rho_D \approx 5.388$ g/cm^3 and $T = 125{,}000$ K. The reflectivity from QMD calculations is also plotted in (c).

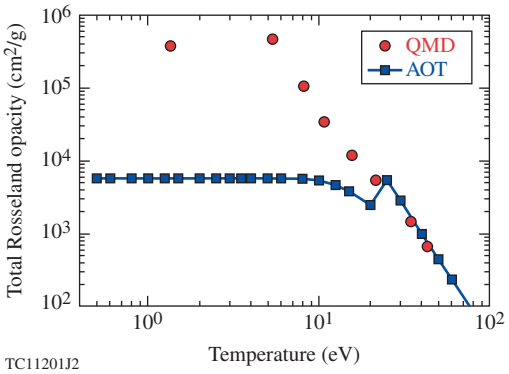

FIG. 4. (Color online) Comparisons of the total Rosseland opacity of deuterium at $\rho_D \approx 5.388$ g/cm^3 as a function of the plasma temperature, between the QMD results (red circles) and the cold-opacity-patched AOT results (blue squares).

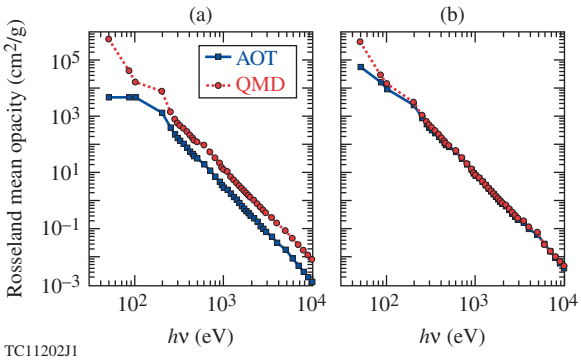

FIG. 5. (Color online) Comparisons of the 48-group Rosseland mean opacity between QMD and AOT as a function of the central photon energy in each group for deuterium of $\rho_D \approx 5.388$ g/cm^3 at temperatures of (a) $T = 10.8$ eV and (b) $T = 43.1$ eV.

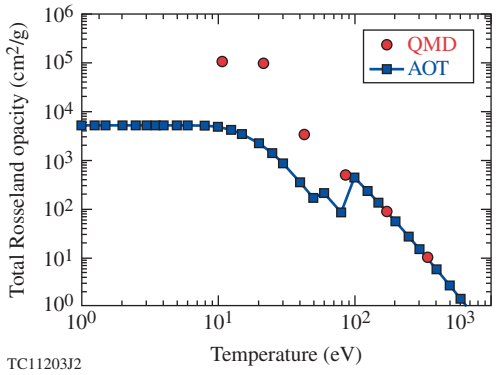

FIG. 6. (Color online) Comparisons of the total Rosseland opacity of deuterium at $\rho_D \approx 199.561$ g/cm^3 as a function of the plasma temperature, between the QMD results (red circles) and the cold-opacity-patched AOT (blue squares).

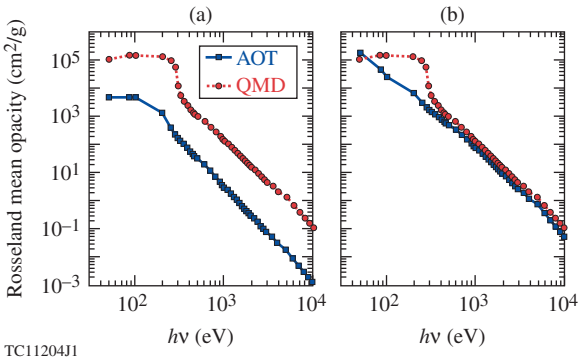

FIG. 7. (Color online) Comparisons of the 48-group Rosseland mean opacity between QMD and AOT as a function of the group photon energy, for deuterium of $\rho_D \approx$ 199.561 g/cm^3 at two different temperatures of (a) $T = 43.1$ eV and (b) $T = 172.3$ eV.

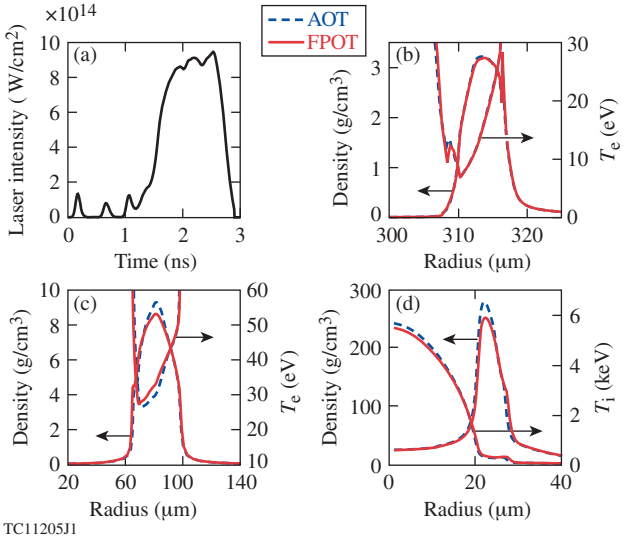

FIG. 8. (Color online) The radiation–hydrodynamics simulation of an OMEGA cryogenic DT implosion ($\alpha = 2.4$) using FPOT (solid red line) is compared with the AOT modeling (dashed blue line): (a) the laser pulse shape; [(b),(c)] the density and electron-temperature profiles of the imploding shell at t = 2.0 ns and t = 2.8 ns, respectively; and (d) the density and ion-temperature profiles at peak compression ($t = 2.98$ ns).

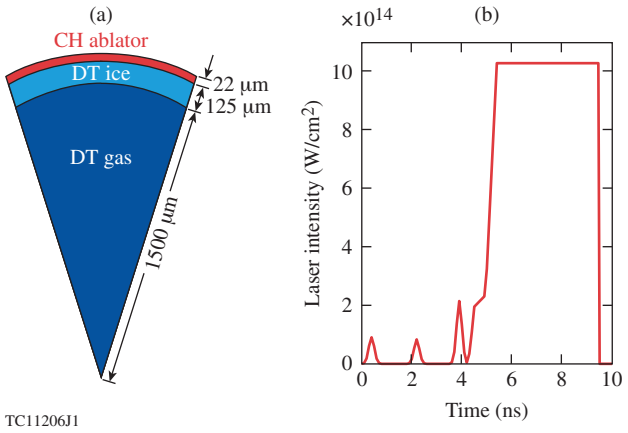

FIG. 9. (Color online) (a) The schematic diagram of a direct-drive NIF target and (b) the laser pulse shape with a total energy of 1.6 MJ, which drives an $\alpha \approx 2.8$ implosion.

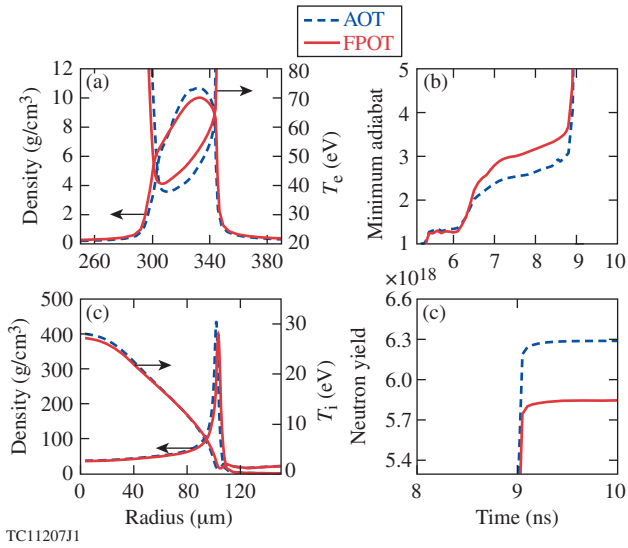

FIG. 10. (Color online) Comparisons of radiation–hydrodynamics simulations between FPOT and AOT modeling, for the direct-drive NIF design shown in Fig. 9: (a) the density and electron-temperature profiles of the imploding shell at t = 8.5 ns, (b) the minimum adiabat as a function of time, (c) the density and ion-temperature profiles at the beginning of burn (t = 8.94 ns), and (d) the neutron yield comparison.

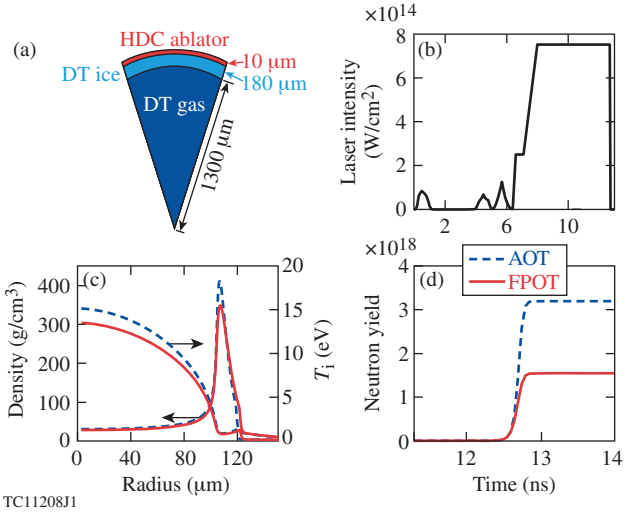

FIG. 11. (Color online) Comparisons of radiation–hydrodynamics simulations between FPOT and AOT modeling for a lower adiabat $\alpha \approx 1.8$), direct-drive NIF design using a high-density–carbon (HDC) ablator: (a) the target dimensions, (b) the triple-picket laser pulse having a total energy of 1.2 MJ, (c) the density and ion-temperature profiles at the beginning of burn ($t = 12.641$ ns), and (d) a comparison of the neutron yields.